JOURNAL OF CHEMICAL & ENGINEERING DATA

ARTICLE

pubs.acs.org/jced

The Melting Curves and Entropy of Iron under High Pressure

Fen Luo,[†] Yan Cheng,[*,†] Xiang-Rong Chen,[*,†,‡] Ling-Cang Cai,[§] and Fu-Qian Jing[§]

[†]College of Physical Science and Technology, Sichuan University, Chengdu 610064, China

[‡]International Centre for Materials Physics, Chinese Academy of Sciences, Shenyang 110016, China

[§]Laboratory for Shock Wave and Detonation Physics Research, Institute of Fluid Physics, Chinese Academy of Engineering Physics, Mianyang 621900, China

ABSTRACT: The melting curves of iron over a wide range of pressures were determined by the molecular dynamics (MD) simulations with the Sutton−Chen version of EAM (embedded atom method). The melting of iron was simulated with two methods, that is, the hysteresis (one-phase) approach and the two-phase approach. Both methods strongly reduced the overheating, and their results are in the close proximity at the applied pressures. The obtained melting curves are consistent with both the diamond anvil cell (DAC) experiments at ambient pressure and the shock wave (SW) measurements at high pressure. During the investigation of the atomic structures of iron, we found a slight increase in the coordination number on melting. When taking account of the ultrapressure melting curves obtained by the Clausius−Clapeyron slope, we found that the starting point is the key to determine the melting curves, and the melting temperatures computed by the Clausius−Clapeyron slope might change dramatically if the initial temperatures change. Finally, the thermal equation of state (EOS) and the pressure dependence of entropy of fusion ΔS of iron have also been obtained.

1. INTRODUCTION

Iron is one of the materials forming the Earth's solid inner core and liquid outer core. Knowledge of the melting properties of iron is of fundamental importance for understanding the Earth's deep interior. At ambient conditions, the ferromagnetic body-centered-cubic (bcc) phase of Fe is the most stable.[1] Early in 1956, the shock compression experiment[2] of the Hugoniot equation of state (EOS) showed that the solid-to-solid phase transformation of iron from bcc to hexagonal-close-packed (hcp) occurred at 13 GPa, which has attracted tremendous experimental and theoretical interest for a long time.[3−6] In general, the hcp phase Fe is stable up to 300 GPa at ambient temperature[7] and up to 3400 K at 100 GPa.[8] Recently, we investigated the magnetism and phase transition of Fe under pressure by the spin-polarized generalized gradient approximation (GGA) within the plane-wave pseudopotential density functional theory (DFT).[9] Our results have shown that the process of the ferromagnetic fcc to the ferromagnetic hcp phase transition, the ferromagnetic bcc to the nonmagnetic hcp phase transition, and the nonmagnetic bcc to nonmagnetic hcp phase transition are 14.4 GPa, 29.5 GPa, and 42.7 GPa, respectively, at ambient temperature. It was also shown that the magnetism can affect the properties of iron up to 72.9 GPa, which confirmed that the nonmagnetic hcp Fe is the most stable structure under higher pressure.[9]

Up to now, many investigations on melting properties of iron have been made experimentally[10−12] and theoretically.[13−17] The phase diagram of iron at high pressure has been investigated through both laser-heated diamond-anvil cell[10,11] and shock-compression experimental techniques.[12] The diamond anvil cell (DAC)[10] melting temperature was linearly extrapolated against density and at 225 GPa was calculated to be about 4360 K. Liao et al.[13] refitted first-principle calculations to the optimized potential model, and obtained a melting temperature of ∼5400 K at 330 GPa. Meantime, Belonoshko et al.[14] determined the melting curve of iron by molecular dynamics (MD) using the Sutton−Chen version of EAM (embedded atom method), and Alfè et al.[16] obtained the melting curve of iron by first-principle calculations. In addition, the Lindemann melting curve of Wang et al.[15] and the dislocation-mediated melting curve of Anderson et al.[17] are in accordance with the DAC data at low pressure and the shock wave (SW) data at high pressure. Liao et al.[13] obtained the melting curve in perfect agreement with old DAC measurements in contrast with SW data. The other theoretical results were consistent with the SW data but diverged with the DAC data at high pressure. They were all inadequate to explain the extreme discrepancies in extrapolating the DAC data to the SW data. Thus, the investigation of the high pressure melting curve of iron will be still a requirement.

Presently, several techniques have been applied to calculate the high-pressure melting curves of crystals, such as the hysteresis (one-phase) approach,[18] the two-phase approach,[19] and the free energy approach.[20] In the one-phase approach, at various pressures, the solid phase is heated until melting, and then the obtained liquid phase is cooled until freezing. The melting temperature is deduced from the temperatures of superheating and supercooling. In the two-phase approach, MD simulations are performed on supercells containing the solid−liquid interface, and superheating could be overcome. In recent years, the two-phase approach has been successfully applied to many materials, such as Fe,[14] LiH,[21] MgO and NaCl,[22] GaN,[23] Ni,[24] He,[25] and so forth. In the free energy approach, the Gibbs energies of the solid and liquid phases are calculated and

Received: October 17, 2010
Accepted: February 25, 2011
Published: March 14, 2011

extrapolated to find the melting temperature by imposing the equality for any fixed pressure. In addition, there exists another method based on calculating the Clausius−Clapeyron slope of the melting transition.[26,27] In the Clausius−Clapeyron slope method, the starting point is the key to determine the melting curves. The choice of different initial fixed points affects the results of the melting curves.

The aim of the present work is as follows. First, we propose to apply the one-phase and two-phase approaches to estimate the high-pressure melting curves of iron in MD simulations. Second, we calculate the thermal EOS, the structure changes in solid and liquid phases, and the entropy of fusion of iron. At last, we investigate the effect of initial temperature on the melting curves obtained by the Clausius−Clapeyron slope method.

2. COMPUTATIONAL METHOD

2.1. Embedded Atom Potential Function. In the MD simulations, we have adopted the Sutton−Chen version of the EAM as the reference model. For the Sutton−Chen version of the EAM model,[14] the model is written as follows:

$$E_{\mathrm{tot}} = \sum_{i=1}^{N} E_i \tag{1}$$

where E_{tot} is the total energy of the system,

$$E_i = \frac{1}{2} \sum_{j=1, j\neq i}^{N} \phi(r_{ij}) + F(\rho_i) \tag{2}$$

$$\rho_i = \sum_{j=1, j\neq i}^{n} \rho(r_{ij}) \tag{3}$$

where $\phi(r)$ is the pairwise interaction between atoms i and j, and r_{ij} is the distance between them. $F(\rho)$ is the embedding function, and ρ is another pairwise function leading to the density term ρ_i. The particular form of the functions ϕ, ρ_i, and $F(\rho)$ is

$$\phi(r_{ij}) = \varepsilon \left(\frac{a}{r_{ij}}\right)^n \tag{4}$$

$$\rho(r_{ij}) = \left(\frac{a}{r_{ij}}\right)^m \tag{5}$$

$$F(\rho_i) = -\varepsilon C \sum_{i=1}^{N} \sqrt{\rho_i} \tag{6}$$

The fitted parameters for iron[14] used in this work are: n = 8.137, m = 4.788, ε = 0.0173 eV, a = 3.4714 Å, and C = 24.939.

2.2. Molecular Dynamics Simulations. All of our calculations were performed with the DL_POLY2.17 program.[28] In the MD simulations, the NPT ensemble[29] was applied to reach constant pressure and temperature. The relaxation times used for the thermostat and the barostat are (1.0 and 0.5) ps, respectively. A potential cutoff distance of 6 Å was applied to van der Waals interactions, and the smooth particle mesh Ewald method[30] was employed with electrostatic interaction. Integration of the equation of motion was performed with a time step of 2 fs; the system was equilibrated for a minimum of 12 ps (6000 time steps), and the statistical averages of the physical properties such as volumes and energies were computed over the remaining time of the 8 ps simulation (4000 time steps). To verify that 12 ps running times were sufficient for our simulations, calculations were performed with different time steps (such as 1 ps, 2 ps, 3 ps, 4 ps, and 5 ps). It was found that our results are fully converged with a time step of 2 fs. The convergence rate of the 2 fs time step is faster than the large time steps.

The one-phase MD simulations started with the supercell (containing a 7 × 7 × 7 unit cell and 686 Fe atoms) constructed from the hcp Fe crystal. This supercell was subjected to incremental heating under the NPT ensemble at a fixed pressure until melting. Then, the obtained liquid Fe is cooled by the same temperature increment until recrystallization. In the two-phase

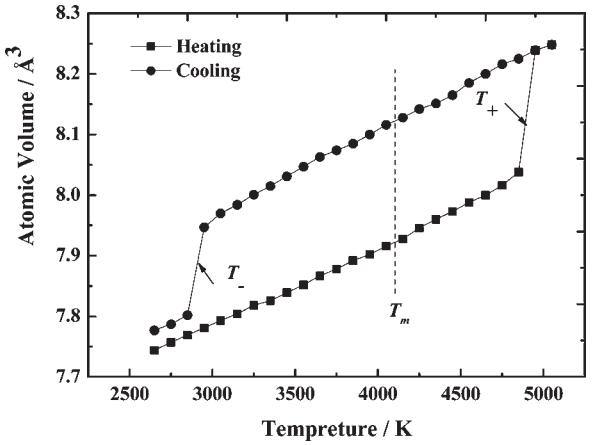

Figure 1. Atomic volume vs temperature during incremental superheating and undercooling process of iron. The melting point T_m can be determined from the superheating and supercooling temperatures T_+ and T_-, respectively, using eq 7.

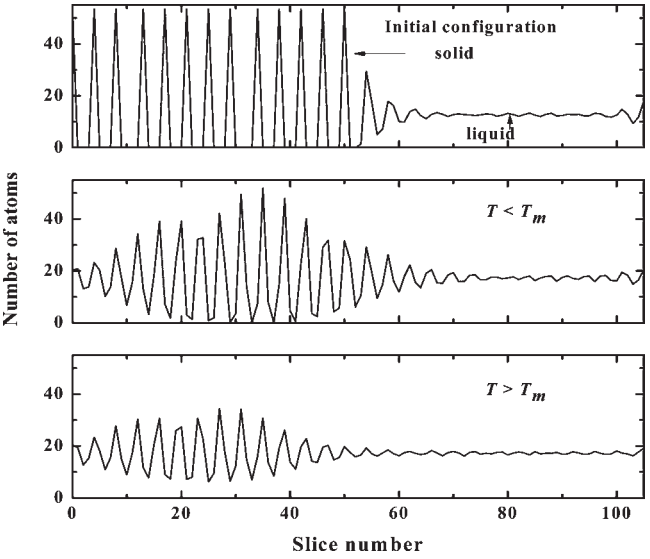

Figure 2. Density profile for the coexistence configuration of one solid phase and one liquid phase. The solid phase is identified by periodic oscillations of the density, while the density of the liquid phase fluctuates randomly with much smaller amplitudes. (a) The initial configuration, (b) the moving of solid−liquid interfaces toward liquid part when $T < T_m$, (c) the moving of solid−liquid interfaces toward solid parts when $T > T_m$. The simulation box contained 1372 atoms, and the slice width was 0.524 Å.

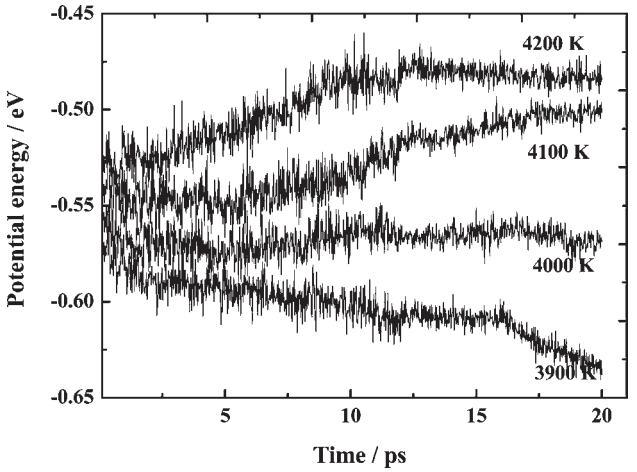

Figure 3. Potential energy per atom of the solid−liquid mixture at various temperatures at 150 GPa in the two-phase simulations.

MD simulations, we started with the supercell (containing a 7 × 7 × 14 unit cell and 1372 Fe atoms) constructed from the hcp structure Fe crystal, froze the half part of the *z*-coordinate of the supercell, and then heated the supercell up to 3000 K (above the melting point) in the NVE ensemble, allowing the Fe atoms at the solid−liquid interface to relax to more stable positions. We obtained the initial configuration containing the solid−liquid interface for further simulations. In the two-phase MD simulations, to check the size effects of the melting temperature, we also started with supercells containing 5 × 5 × 10, 6 × 6 × 12, and 7 × 7 × 14 unit cells of the hcp Fe crystal. Our simulation results indicate that convergence of the melting temperature is achieved with the super cell having a 7 × 7 × 14 unit cell.

2.3. Equilibrium Melting Point. In the one-phase approach, the supercell is simulated in isothermal−isobaric (NPT) ensembles. When we incrementally heated the supercell, a sudden jump in volume was found upon reaching the melting temperature T_+. Also, a drop in the volume could be seen at T_- in a cooling simulation of liquid Fe. The volume−temperature ($V-T$) curve (Figure 1) reveals the hysteresis effects. The equilibrium melting temperature T_m can be deduced from the maximum degree of superheating (T_+) and supercooling (T_-)[31,32]

$$T_m = T_+ + T_- - \sqrt{T_+ T_-} \quad (7)$$

The two-phase MD simulations can also be used to obtain the melting temperature T_m.[24,33] In Figure 2a, we show the initial configuration with an average number density in slices of the supercell parallel to the solid−liquid interface. The solid phase is identified by periodic oscillations of the number density, while the number density of the liquid phase fluctuates randomly with much smaller amplitudes. Under a fixed pressure, when the system temperature is below the melting point, the solid−liquid interface will move toward the liquid part (Figure 2b), whereas it moves toward the solid parts when the temperature is above the melting point (Figure 2c). By narrowing the interval, the melting temperature can be obtained at a specific pressure. On the other hand, the melting temperature can also be determined by the potential energy evolution at various temperatures (Figure 3). Over the duration of the simulation, the potential energy of the system remains constant at the melting temperature. When the temperatures are above the equilibrium melting point, the potential energy increases due to the solid part progressively melting. When the temperatures are lower than the equilibrium melting point, the potential energy decreases due to more liquid continuously crystallizing. We can judge the temperature either below or above melting point at a fixed pressure by monitoring the change of the potential energy. Then, we narrowed the range of the melting temperature at this pressure. Repeating the above steps, we can obtain the whole melting curve within the applied pressures.

Table 1. Melting Temperatures of Fe under High Pressure from the One-Phase Approach

P	T_+	T_-	T_m		
GPa	K	K	K	θ_c^+	θ_c^-
60	2875.0	1675.0	2355.5	1.22	0.71
100	3900.0	2300.0	3205.0	1.22	0.72
150	4900.0	2900.0	4030.4	1.22	0.72
200	6000.0	3600.0	4952.4	1.21	0.73
250	6900.0	4100.0	5681.2	1.21	0.72

3. RESULTS AND DISCUSSION

3.1. High Pressure Melting. With the one-phase approach, we calculated the melting temperatures of Fe up to 250 GPa (Table 1). In our simulations, at different pressures, we observed the incremental superheating and supercooling with a heating and cooling rate of 2.5 K·ps^{-1}. The supercell remained superheated before melting in the heating process and undercooled before crystallizing in the cooling process. To quantify the degree of superheating and undercooling, we explored the maximum superheating and supercooling defined as: $\theta_c^+ = T_+/T_m$, $\theta_c^- = T_-/T_m$, where T_+ is the highest temperature achieved in the superheated solid, T_- is the lowest temperature in the undercooled liquid, and T_m is the melting temperature determined from eq 7. We found that θ_c^+ and θ_c^- are respectively 1.22 ± 0.01 and 0.72 ± 0.01 and keep constant regardless of pressure. Belonoshko et al.[34] showed the superheating (coefficient called k_{AB}) of monatomic solids at high pressure is 1.23; our results support their calculations.

Our melting curves of Fe are shown in Figure 4 compared with experiments and other calculations. At 60 GPa, the melting point of the two-phase method is (2425 ± 25) K, which is in excellent agreement with the value, (2355 ± 50) K, of the one-phase method. At lower pressures around (60 to 80) GPa, our two melting curves both agree with the DAC values.[10,11] At higher pressure, our two melting curves all diverge from the DAC values as well as other theoretical results[14−17] with increasing pressure. The melting temperature of Ma et al.[11] shifted upward by about 700 K at 105 GPa compared with the old DAC experiment.[10] At 200 GPa, our melting temperature from the two-phase method is 4950 K, which is consistent with the shock temperature (5100 ± 500) K at 225 GPa.

In the shock experiment, we can determine the melting temperature through the abrupt decrease of the acoustic velocity with increasing shock compressions. Jeffrey and Holmes[12] show the shock wave melting temperature is (5100 ± 500) K at 225 GPa. The melting temperatures measured from DAC experiments are often lower than those from SW experiments.

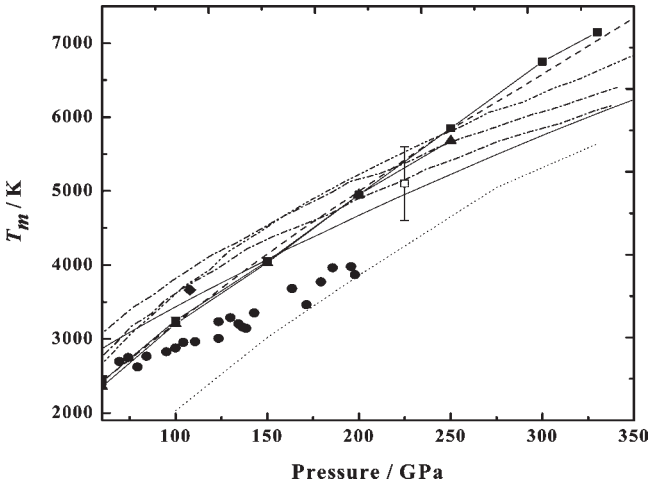

Figure 4. Melting curves obtained with the hysteresis method (▲) and two-phase simulations (■) in comparison with DAC measurements of Boehler et al. in ref 10, ●; Ma et al. in ref 11, ◆; shock wave melting temperature of Jeffrey et al. in ref 12, □. Theoretical simulated melting curves by Liao et al. in ref 13, dotted line; dashed line, Belonoshko et al. in ref 14; dash−dot−dot line, Wang et al. in ref 15, dash−dot line, Alfé et al. in ref 16; solid line, Anderson et al. in ref 17.

Belonoshko et al.[35] showed a generic scenario when measuring melting temperatures in a DAC. It is known, when the resistance to the shear of a material is low, the material yields to the stress, which can be observed before the melting occurs. The phenomenon is often mistaken as the melting. Indeed, a number of melting curves obtained by the DAC method are low, particularly for transition metals (Fe, Ta, Mo, etc.), as compared to the most precise theoretical assessments and shock measurements.[36]

The theoretical results from first-principle methods, MD simulation, and empirical melting models (including Lindemann law and dislocation-mediated melting models) mainly offer support to the shock wave melting temperatures. However, the results of Liao et al.[13] tended to support the DAC experiments. These various theoretical methods have their own advantages and disadvantages, even if the results of different theoretical methods differ largely, especially in the high pressure region. The first-principle method is still challenging due to the heavy computational demand, but the accurate computation of a wide range of physical properties has been accepted widely. The MD simulation is applied to a large system and run with the potentials of the summation of atomic interaction potentials, which are fitted to the atomic configurations of the experimental and the first-principle data. In this work, we applied the Sutton−Chen version of EAM, which has been successfully applied to the structure of liquid Fe at high pressure.[37,38] When the empirical melting models have been used for iron,[15,17] different melting temperatures have been observed. If the starting parameters are slightly modified, the dislocation melting model can give large differences for the melting temperatures of transition metals.[39] In addition, the Lindemann law is also an empirical law based on earlier experimental investigations of simple gases at low pressure, whereas it may be a debated issue when it is used to model a complex metal under high pressure. Although each method can describe or explain the melting properties of Fe from different aspects, all of the theoretical methods have their own limitations to describe the ultrahigh pressure properties.

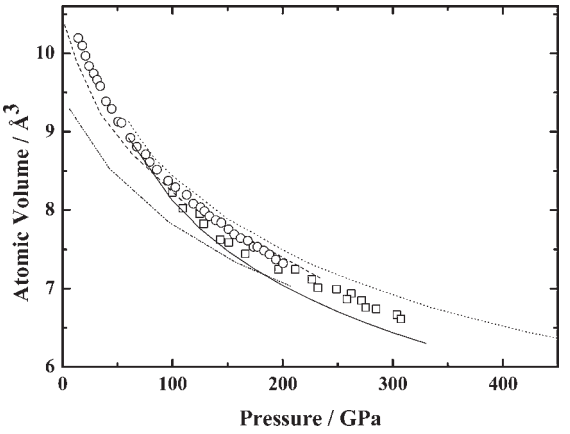

Figure 5. The 300 K isotherm experimental measurements of Mao et al. in ref 49 □; dotted line, Dubrovinsky et al. in ref 50 and ◇, Dewaele et al. in ref 51. The previous calculations 300 K isotherm of Dewaele et al. in ref 51 with PAW-LDA (dash−dot−dot line) and PAW-GGA (dash line). Solid line, the 300 K isotherm for hcp Fe obtained in this work.

We should overcome the Gibbs energy barrier to the formation of a nucleus of a daughter phase when the solid−liquid transitions begin with nucleation.[33] The two-phase simulation can solve the problem of superheating, as the solid−liquid interface assists in the nucleation in the melting or crystallization process. In the present simulations, we noted that the one-phase can also eliminate superheating, and the melting curves from both methods are nearly identical. We treated Fe as an ideal solid and liquid at the beginning of the simulations and ignored the local structures of the supercell during simulations. The short-range order (SRO) structure is in effect impurities in the liquid and is likely to influence the melting of a metal. The measurements of Schenk et al.[40] and Lee et al.[41] demonstrated the icosahedral short-range order (ISRO) in melting iron. For other metals, such as Ni, Ta, and Zr,[42−45] one also observes the ISRO in theory.

At present, the conflict among the DAC, SW, and theoretical results is still existent. A possible resolution of the conflict has emerged recently for Mo and Ta.[36,46−48] Thus, we thought that there may exist new phases in both solid and liquid Fe under high pressures and temperatures. The high pressure melting curve of Fe still remains inconclusive. More experimental measurements and theoretical calculations are urgently necessary to further determine the phases and then the whole melting curve.

3.2. Thermal Equation of State. To determine the EOS of iron, MD simulations were performed on an NPT ensemble at various temperatures and pressures. The calculated isothermal compression curves are shown in Figure 5, together with the experimental data[49−51] and other calculations.[51] One notes that the atomic volume compression is 29.3 % from (60 to 330) GPa. In the low-pressure range [(60 to 100) GPa], the results are in accordance with the experiments.[49,51] Above 100 GPa, our results deviate a little from the experimental results at high pressure (less than 4 %). Our calculations roughly reproduce the trend of a pressure-induced reduction in volume observed in the experiments.[49−51] The dispersion in our simulations might be due to that we only considered pure crystals in our simulation, whereas impurities do exist in the experimental samples, and there are also some experimental limitations. Another reason is that the MD simulations ignore the electronic entropy both

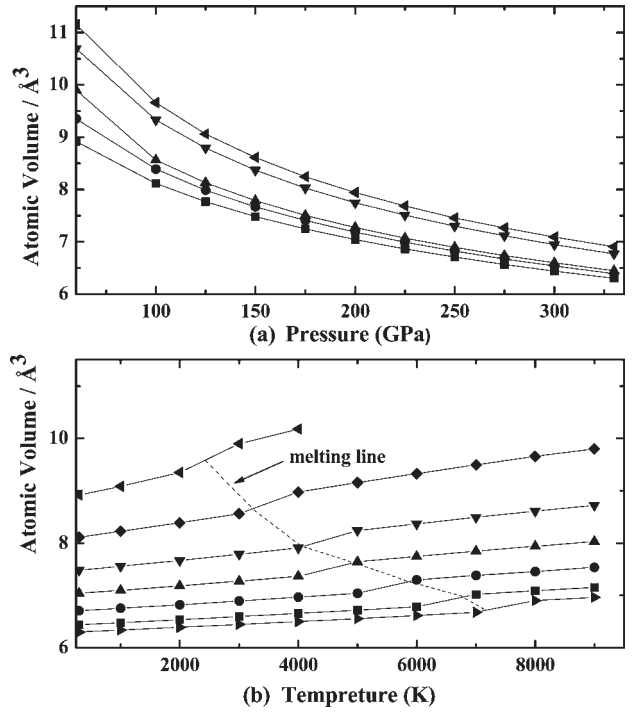

Figure 6. (a) Isotherms of iron at different temperatures: ■, 300 K; ●, 2000 K; ▲, 3000 K;▼, 6000 K; solid left-pointing triangle, 8000 K. (b) Isobars of iron at different pressures: solid left-pointing triangle, 60 GPa; ◆, 100 GPa; ▼, 150 GPa; ▲, 200 GPa; ●, 250 GPa; ■, 300 GPa; solid right-pointing triangle, 330 GPa.

for the solid and liquid phases,[52] which is important at high temperatures.

The $P-V-T$ equations of state (EOS) for crystalline materials are of importance in many applications. It can provide a convenient measure of the thermodynamic properties, such as thermal expansivity and bulk modulus. In Figure 6, we illustrate the isotherms and isobar curves in the range of (0 to 330) GPa and temperatures up to 9000 K. The isothermal compressibilities of Fe showed the effect of increasing pressure on Fe is the same as that of decreasing temperature (Figure 6a). As the pressure increases, the atomic volume decreases at the given temperature, and the values of atomic volume at lower temperature are less than that at higher temperature at the same pressure. As for the isobaric curves shown in Figure 6b, we see that, under lower pressure, the volume varies quickly as the temperature rises. Under higher pressures, it becomes moderate, and the curves are nearly linear. Along isobars the atomic volumes jump dramatically with increasing pressure, which means that the solid Fe melts along isobars when the temperature is increased above the melting temperature.

3.3. Atomic Structure of Solid and Liquid Fe. The atomic structures of the liquid and solid Fe remain quite distinct: the solid Fe is of long-range order, but the liquid Fe is of short-range order. The radial distribution function (RDF), $g(r)$, is very important in understanding the atomic structure of solid and liquid Fe. The RDF is defined by

$$g(r) = \frac{N_n(r)V_n}{4\pi r^2 dr N} \tag{8}$$

where N is the number of atoms, V_n and $N_n(r)$ are the mean volume and mean numbers of atoms between r and $r + \Delta r$ from

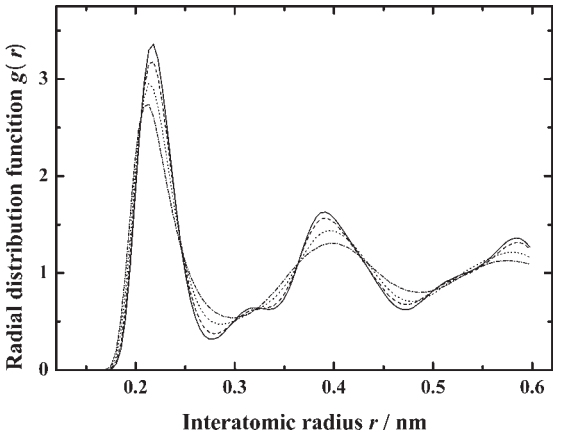

Figure 7. The radial distribution function (RDF) of iron for: solid at P = 150 GPa and T = 3800 K (solid line), 3900 K (dashed line), and 4000 K (dotted line), liquid at P = 150 GPa and T = 4100 K (dash−dot line), respectively.

an atom. To investigate the behavior of the atomic structure, we ran the MD simulations at a number of temperatures ranging from (3800 to 4100) K at 150 GPa. The comprehensive analysis of the RDF can provide a deeper insight into the structure information, such as bond length, atomic bond angle distributions, crystalline system, and coordination numbers.

Figure 7 illustrates our RDF $g(r)$ at 3800 K, 3900 K, 4000 K, and 4100 K. In the solid phase [(3800 to 4000) K], the distributions exhibit their first distinctive peaks around (2.17, 2.17, and 2.17) Å. Clearly, as the temperature increases, there is no effect of temperature on the position of the first peak, while the second peak starts to vanish due to the first and second peaks merging. The third and higher neighbors in the solid become heavily broadened in the liquid phase, and the change in $g(r)$ going from the solid at 4000 K to the liquid at 4100 K is shown by well-defined peaks. This behavior is expected for melting and can be compared to the increased disorder at melting.

The running coordination number (RCN), N_c, can be calculated from the RDF, $g(r)$, by means of the following equation:

$$N_c = 4\pi\overline{\rho}\int_0^{r_c} g(r)r^2 dr \tag{9}$$

where is the bulk number density and r_c is the interatomic distance. Figure 8 shows a comparison between the running coordination number in the solid phase at 3800 K, 3900 K, and 4000 K, and in the liquid phase at 4100 K. The distances to the first minimum at four temperatures are (2.78, 2.78, 2.78, and 2.97) Å, and the corresponding coordination numbers N_c are 12, 12, 12, and 13. Therefore, apart from the expected disorder in Fe on melting, the change of coordination number of Fe on melting is a slight increase. Koči et al.[53] also found an increase in the coordination number for Na during melting. Early in 1972, Ross and Miller[54] presented a correlation between the coordination number and the volume change on melting. Our results show that the effect of the volume change of Fe upon melting on the coordination number is not more obvious than that of Na.[53]

3.4. Entropy of Fusion. In the MD simulation, several thermodynamic properties for the solid and liquid phases at T_m as a function of pressure can be conducted. The change of

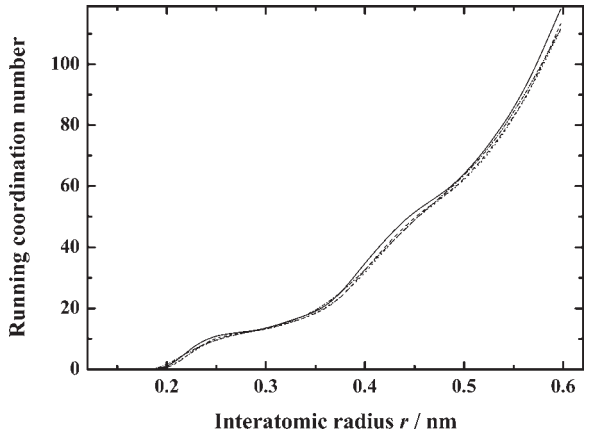

Figure 8. The running coordinate number (RCN) of iron for: solid at P = 150 GPa and T = 3800 K (solid line), 3900 K (dashed line), and 4000 K (dotted line), liquid at P = 150 GPa and T = 4100 K (dash−dot line), respectively.

Table 2. Enthalpies for Liquid and Solid H_L and H_S, Entropy of Fusion ΔS, Molar Volumes for Liquid and Solid V_L and V_S, and the Molar Volume Change ΔV at the Melting Point

P	H_L	H_S	ΔS	V_L	V_S	ΔV
GPa	eV	eV	(k_B)	$cm^3 \cdot mol^{-1}$	$cm^3 \cdot mol^{-1}$	$cm^3 \cdot mol^{-1}$
60	1369.6	1249.4	0.8630	5.856	5.697	0.159
100	3010.4	2849.8	0.8477	5.320	5.183	0.137
150	4857.4	4657.2	0.8403	4.887	4.767	0.120
200	6614.8	6372.0	0.8294	4.601	4.490	0.111
250	8290.8	8012.7	0.8281	4.387	4.283	0.104

Gibbs energy $G = H - TS$ is zero in the solid−liquid coexisting equilibrium,

$$\Delta G = \Delta H - T\Delta S = 0 \tag{10}$$

where S is the entropy and H is the enthalpy. Then, the entropy of fusion ΔS is defined by

$$\Delta S = \frac{\Delta H}{T_m} = \frac{H_L - H_S}{T_m} \tag{11}$$

where H_L and H_S are the enthalpies for the liquid and solid phases at the melting point T_m, respectively. In the NPT ensemble, we heated the supercell (containing 686 Fe atoms) incrementally up to high temperatures and then cooled at fixed pressure. Then we can evaluate the thermodynamic properties at the melting point T_m. The results are presented in Table 2. We can note that the enthalpies of the liquid and solid phases at the melting point increase with pressure, and the enthalpy of the liquid is a little larger than the solid at a given pressure. As the pressure increases, the molar volumes of liquid and solid, V_L and V_S, will decrease. The molar volume of liquid is larger than that of solid at the same pressure.

Now, we focus on the entropy of fusion ΔS of Fe under high pressure in Figure 9a, where the first-principle value of Alfè et al is also shown.[55] Our value of ΔS is 0.8477k_B at 100 GPa, well in accordance with the calculations, 0.85k_B at 127 GPa. We find that the entropy of fusion ΔS changes a little with pressure from about

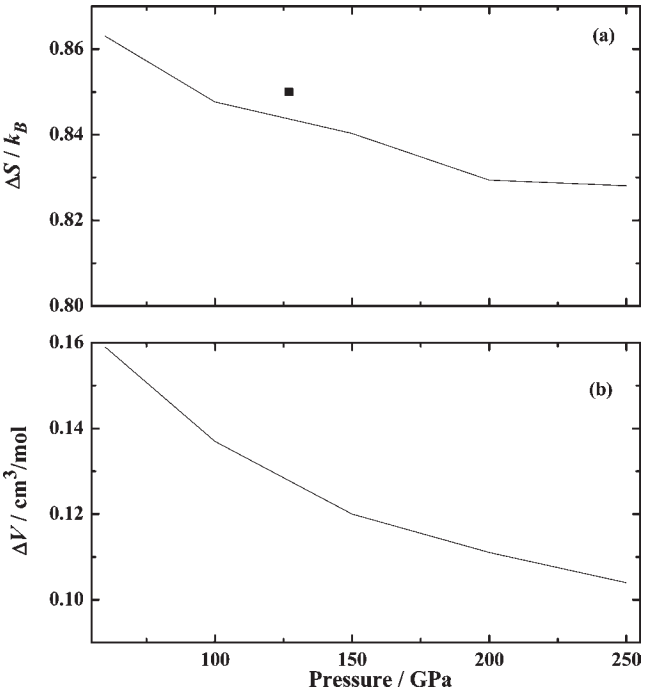

Figure 9. (a) Entropy change on melting per atom (units of Boltzmann's constant k_B) as a function of pressure; ■, ref 55; (b) Molar volume change on melting as a function of pressure.

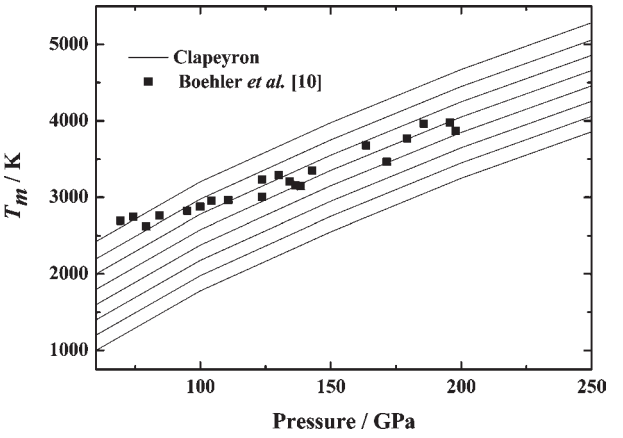

Figure 10. Melting curves of iron from the Clausius−Clapeyron slope, assuming a number of initial fixed points at ambient pressure, compared with the experimental data.[10]

0.8630k_B at 60 GPa to about 0.8281k_B at 250 GPa. The molar volume change ΔV at different pressures are shown in Figure 9b. As the pressure P increases, the molar volume change ΔV decreases, which is more of an effect than the entropy of fusion ΔS.

The slope of the melting curve was calculated using the Clausius−Clapeyron equation:

$$\frac{dP}{dT} = \frac{\Delta H}{T\Delta V} \tag{12}$$

where ΔH is the difference enthalpy between the coexisting phases, while ΔV is the difference in volume. We solved the eq 12 by performing the NPT simulations for the solid and liquid phase and then evaluating ΔH and ΔV. We verified the possible initial

fixed point effect in the ultrapressure melting curves. All of the results obtained for the melting curves of iron are summarized in Figure 10, together with the experimental values.[10] We see that the choice of different initial fixed points will affect the results of the melting curves. If we assume the initial temperature is 2000 K, the melting curves are in good agreement with experiment at high pressure.[10] When the initial temperature is taken as 2425 K, the melting curves will coincide with the low-pressure experimental values.[10] It is found that the melting temperatures computed by the Clausius−Clapeyron slope might change dramatically if the initial temperatures change.

4. CONCLUSIONS

In summary, we have deployed molecular dynamics to compute the melting properties, thermal EOS, atomic structure of solid and liquid, and the entropy of fusion of the hcp Fe structure. We have compared the two techniques commonly used to calculate the melting curve of a material with MD simulations, namely, the hysteresis (one-phase) approach and the two-phase approach. Both methods strongly reduced the overheating, and they are nearly identical over the applied pressure. The obtained melting curves are consistent with experiments at low pressures and shock wave melting at high pressure. The large discrepancy between the extrapolated DAC results and shock wave melting temperatures still exists, so the condition of experimental measurement should be modified to further determine the phase and the ultrahigh-pressure melting curves. When taking account of the ultrapressure melting curves obtained by the Clausius−Clapeyron slope, we found that the starting point is the key to determine the melting curves, and the melting temperatures computed by the Clausius−Clapeyron slope might change dramatically if the initial temperatures change. Finally, the thermal EOS and the entropy of fusion ΔS as a function of pressure have been also obtained successfully.

AUTHOR INFORMATION

Corresponding Author

*E-mail: ycheng@scu.edu.cn (Y. Cheng); x.r.chen@tom.com (X.-R. Chen).

Funding Sources

We also thank the support by the National Natural Science Foundation of China (Grant Nos. 10776022 and 10776029) and the Specialized Research Fund for the Doctoral Program of Higher Education under Grant No. 20090181110080.

ACKNOWLEDGMENT

The authors would like to thank Prof. Dr. Dario Alfè for his useful suggestions.

REFERENCES

(1) Hasegawa, H.; Pettifor, D. G. Microscopic Theory of the Temperature-Pressure Phase Diagram of Iron. *Phys. Rev. Lett.* **1983**, *50*, 130.

(2) Bancroft, D.; Peterson, E. L.; Minshall, S. Polymorphism of Iron at High Pressure. *J. Appl. Phys.* **1956**, *27*, 291.

(3) Saxena, S. K.; Shen, G.; Lazor, P. Temperatures in the Earth's Core Based on Melting and Phase Transformation Experiments on Iron. *Science* **1994**, *264*, 405.

(4) Kalantar, D. H.; Belak, J. F.; Collins, G. W.; Colvin, J. D.; Davies, H. M.; Eggert, J. H.; Germann, T. C.; Hawreliak, J.; Holian, B. L.; et al. Direct Observation of the α-ε Transition in Shock-Compressed Iron via Nanosecond X-Ray Diffraction. *Phys. Rev. Lett.* **2005**, *95*, 075502.

(5) Kadau, K.; Germann, T. C.; Lomdahl, P. S.; Holian, B. L. Atomistic simulations of shock-induced transformations and their orientation dependence in bcc Fe single crystals. *Phys. Rev. B* **2005**, *72*, 064120.

(6) Friák, M.; Šob, M. *Ab initio* study of the bcc-hcp transformation in iron. *Phys. Rev. B* **2008**, *77*, 174117.

(7) Hemley, R. J.; Mao, H. K. *In Situ* Studies of Iron under Pressure: New windows on the Earth's Core. *Int. Geol. Rev.* **2001**, *43*, 1.

(8) Karato, S. Inner Core Anisotropy Due to the Magnetic Field—induced Preferred Orientation of Iron. *Science* **1993**, *262*, 1708.

(9) Zeng, Z. Y.; Hu, C. E.; Chen, X. R.; Cai, L. C.; Jing, F. Q. Magnetism and phase transitions of iron under pressure. *J. Phys.: Condens. Matter* **2008**, *20*, 425217.

(10) Boehler, R. Temperatures in the Earth's core from melting-point measurements of iron at high static pressures. *Nature* **1993**, *363*, 534.

(11) Ma, Y. Z.; Somayazulu, M.; Shen, G.; Mao, H. K.; Shu, J.; Hemley, R. In situ X-ray diffraction studies of iron to Earth-core conditions. *Phys. Earth Planet. Inter.* **2004**, *143*, 455.

(12) Jeffrey, H. N.; Holmes, N. C. Melting of iron at the physical conditions of the Earth's core. *Nature* **2004**, *427*, 339.

(13) Laio, A.; Bernard, S.; Chiarotti, G. L.; Scandolo, S.; Tosatti, E. Physics of Iron at Earth's Core Conditions. *Science* **2000**, *287*, 1027.

(14) Belonoshko, A. B.; Ahuja, R.; Johansson, B. Quasi−*Ab Initio* Molecular Dynamic Study of Fe Melting. *Phys. Rev. Lett.* **2000**, *84*, 3638.

(15) Wang, Y.; Ahuja, R.; Johansson, B. Melting of iron and other metals at earth's core conditions: A simplified computational approach. *Phys. Rev. B* **2001**, *65*, 014104.

(16) Alfè, D.; Price, G. D.; Gillan, M. J. Thermodynamics of hexagonal-close-packed iron under Earth's core conditions. *Phys. Rev. B* **2002**, *65*, 165118.

(17) Anderson, O. L.; Isaak, D. G.; Nelson, V. E. The high-pressure melting temperature of hexagonal close-packed iron determined from thermal physics. *J. Phys. Chem. Solids* **2003**, *64*, 2125.

(18) Luo, S. N.; Ahrens, T. J.; Cağin, T.; Strachan, A.; Goddard, W. A., III; Swift, D. C. Maximum superheating and undercooling: Systematics, molecular dynamics simulations, and dynamic experiments. *Phys. Rev. B* **2003**, *68*, 134206.

(19) Belonoshko, A. B. Molecular dynamics of $MgSiO_3$ perovskite at high pressures: Equation of state, structure, and melting transition. *Geochim. Cosmochim. Acta* **1994**, *58*, 4039.

(20) Gillan, M. J.; Alfè, D.; Brodholt, J.; Vocadlo, L.; Price, G. D. First-principles modelling of Earth and planetary materials at high pressures and temperatures. *Rep. Prog. Phys.* **2006**, *69*, 2365.

(21) Ogitsu, T.; Schwegler, E.; Gygi, F.; Galli, G. Melting of Lithium Hydride under Pressure. *Phys. Rev. Lett.* **2003**, *91*, 175502.

(22) Belonoshko, A. B.; Dubrovinsky, L. S. Molecular dynamics of NaCl (B1 and B2) and MgO (B1) melting; two-phase simulation. *Am. Minerals* **1996**, *81*, 303.

(23) Harfuji, K.; Tsuchiya, T.; Kawamura, K. Molecular dynamics simulation for evaluating melting point of wurtzite-type GaN crystal. *J. Appl. Phys.* **2004**, *96*, 2501.

(24) Luo, F.; Chen, X. R.; Cai, L. C.; Ji, G. F. Solid−liquid interfacial energy and melting properties of nickel under pressure from molecular dynamics. *J. Chem. Eng. Data* **2010**, *55*, 5149–5155.

(25) Koči, L.; Ahuja, R.; Belonoshko, A. B.; Johansson, B. Study of the high-pressure helium phase diagram using molecular dynamics. *J. Phys.: Condens. Matter* **2007**, *19*, 016206.

(26) Strachan, A.; Cagin, T.; Goddard, W. A., III. Phase diagram of MgO from density-functional theory and molecular-dynamics simulations. *Phys. Rev. B* **1999**, *60*, 15084.

(27) de Koker, N.; Stixrude, L. Self-consistent thermodynamic description of silicate liquids, with application to shock melting of MgO periclase and $MgSiO_3$ perovskite. *Geophys. J. Int.* **2009**, *178*, 162.

(28) Smith, W.; Forrester, T. R.; Todorov, I. T.; Leslie, M. *The DL_POLY_2 user manual, version 2.17*; The Council for the Central Laboratory of Research Councils: Daresbury Laboratory, Warrington, Cheshire, UK, 2006.

(29) Berendsen, H. J. C.; Postma, J. P. M.; Gunsteren, W. v.; DiNola, A.; Haak, J. R. Molecular dynamics with coupling to an external bath *J. Chem. Phys.* **1984**, *81*, 3684.

(30) Essmann, U.; Perera, L.; Berkowitz, M. L.; Darden, T.; Lee, H.; Pederson, L. G. A smooth particle mesh Ewald method. *J. Chem. Phys.* **1995**, *103*, 8577.

(31) Luo, S. N.; Ahrens, T. J. Superheating systematics of crystalline solids. *Appl. Phys. Lett.* **2003**, *82*, 1836.

(32) Zheng, L.; Luo, S. N.; Thompson, D. L. Molecular dynamic simulations of melting and glass transition of nitromethane. *J. Chem. Phys.* **2006**, *124*, 154504.

(33) Luo, S. N.; Strachan, A.; Swift, D. C. Nonequilibrium melting and crystallization of a model Lennard-Jones system. *J. Chem. Phys.* **2004**, *120*, 11640.

(34) Belonoshko, A. B.; Skordumova, N. V.; Rosengren, A.; Johansson, B. Melting and critical superheating. *Phys. Rev. B* **2006**, *73*, 012201.

(35) Belonoshko, A. B.; Ahuja, R.; Johansson, B. Molecular dynamics of LiF melting. *Phys. Rev. B* **2000**, *61*, 11928.

(36) Belonoshko, A. B.; Burakovsky, L.; Chen, S. P.; Johansson, B.; Mikhaylushkin, A. S.; Preston, D. L.; Simak, S. I.; Swift, D. C. Molybdenum at High Pressure and Temperature: Melting from Another Solid Phase. *Phys. Rev. Lett.* **2008**, *100*, 135701.

(37) Koči, L.; Belonoshko, A. B.; Ahuja, R. Molecular dynamics study of liquid iron under high pressure and high temperature. *Phys. Rev. B* **2006**, *73*, 224113.

(38) Koči, L.; Belonoshko, A. B.; Ahuja, R. Molecular dynamics calculation of liquid iron properties and adiabatic temperature gradient in the Earth's outer core. *Geophys. J. Int.* **2007**, *168*, 890.

(39) Errandonea, D. Comment on "Theoretical solid and liquid state shock Hugoniots of Al, Ta, Mo and W". *J. Phys.: Condens. Matter* **2004**, *16*, 8801.

(40) Schenk, T.; Holland-Moritz, D.; Simonet, V.; Bellissent, R.; Herlach, D. M. Icosahedral Short-Range Order in Deeply Undercooled Metallic Melts. *Phys. Rev. Lett.* **2002**, *89*, 075507.

(41) Lee, G. W.; Gangopadhyay, A. K.; Kelton, K. F.; Hyers, R. W.; Rathz, T. J.; Rogers, J. R.; Robinson, D. S. Difference in Icosahedral Short-Range Order in Early and Late Transition Metal Liquids. *Phys. Rev. Lett.* **2004**, *93*, 037802.

(42) Jakse, N.; Pasturel, A. Ab initio molecular dynamics simulations of local structure of supercooled Ni. *J. Chem. Phys.* **2004**, *120*, 6124.

(43) Jakse, N.; Pasturel, A. Molecular-dynamics study of liquid nickel above and below the melting point. *J. Chem. Phys.* **2005**, *123*, 244512.

(44) Jakse, N.; Bacq, O. Le.; Pasturel, A. Prediction of the local structure of liquid and supercooled tantalum. *Phys. Rev. B* **2004**, *70*, 174203.

(45) Jakse, N.; Pasturel, A. Local Order of Liquid and Supercooled Zirconium by *Ab Initio* Molecular Dynamics. *Phys. Rev. Lett.* **2003**, *91*, 195501.

(46) Cazorla, C.; Alfè, D.; Gillan, M. J. Comment on "Molybdenum at High Pressure and Temperature: Melting from Another Solid Phase". *Phys. Rev. Lett.* **2008**, *101*, 049601.

(47) Mikhaylushkin, A. S.; Simak, S. I.; Burakovsky, L.; Chen, S. P.; Johansson, B.; Preston, D. L.; Swift, D. C.; Belonoshko, A. B. Mikhaylushkin et al. Reply. *Phys. Rev. Lett.* **2008**, *101*, 049602.

(48) Burakovsky, L.; Chen, S. P.; Preston, D. L.; Belonoshko, A. B.; Rosengren, A.; Mikhaylushkin, A. S.; Simak, S. I.; Moriatry, J. A. High-Pressure—High-Temperature Polymorphism in Ta: Resolving an Ongoing Experimental Controversy. *Phys. Rev. Lett.* **2010**, *104*, 255702.

(49) Mao, H. K.; Wu, Y.; Chen, L.; Shu, J.; Jephcoat, A. P. Static compression of iron to 300 GPa and $Fe_{0.8}Ni_{0.2}$ alloy to 260 GPa: implications for composition of the core. *J. Geophys. Res.* **1990**, *95* 21737.

(50) Dubrovinsky, L. S.; Saxena, S. K.; Tutti, F.; Rekhi, S.; LeBehan, T. *In Situ* X-Ray Study of Thermal Expansion and Phase Transition of Iron at Multimegabar Pressure. *Phys. Rev. Lett.* **2000**, *84*, 1720.

(51) Dewaele, A.; Torrent, M.; Loubeyre, P.; Mezouar, M. Compression curves of transition metals in the Mbar range: Experiments and projector augmented-wave calculations. *Phys. Rev. B* **2008**, *78*, 104102.

(52) Wasserman, E.; Stixrude, L.; Cohen, R. E. Thermal properties of iron at high pressures and temperatures. *Phys. Rev. B* **1996**, *53*, 8296.

(53) Koči, L.; Ahuja, R.; Vitos, L.; Pinsook, U. Melting of Na at high pressure from *ab initio* calculations. *Phys. Rev. B* **2008**, *77*, 132101.

(54) Ross, J. W.; Miller, W. A. Random packing model of liquid metals at their melting temperatures. *Can. Metall. Q* **1972**, *11*, 459.

(55) Alfè, D.; Price, G. D.; Gillan, M. J. The melting curve of iron from quantum mechanics calculations. *J. Phys. Chem. Solids* **2004**, *65*, 1573.